

Modeling of Atmospheric Effects on Terahertz Imaging Systems

Sean G. O'Brien and David H. Tofsted
U.S. Army Research Laboratory
Computational and Information Sciences Directorate
White Sands Missile Range, New Mexico 88002
sobrien@arl.army.mil
Ph: (505) 678-1570
FAX: (505) 678-3385

Abstract

The terahertz (THz) electromagnetic frequency band is a potentially useful domain for remote sensing in military and Homeland Security applications. Sensors operating in this band gain some of the material penetrating abilities of radio waves, some of the image resolving capabilities of infrared (IR) devices, and an enhanced chemical discrimination capacity inherent to the THz band itself. Both passive (thermal) and active (maser) THz sensor operating modes have been contemplated, with the greatest emphasis on active sensors. Active sensors gain a particular advantage due to typical equivalent source brightness temperatures in the neighborhood of 10^{18} K. At these intensities, the significance of natural emission effects is negligible, but the influence of water vapor absorption can be significant at frequencies above 0.4 THz. For systems performance analysis we have developed simulation software to assess the limiting effects of the atmosphere on both passive and active terahertz imagers for various instrumental operating frequencies, bandwidths, sensor noise levels, integration times, and atmospheric conditions. We will show some of the early results of our modeling and simulation efforts, which illustrate the wide range of potential for atmospheric impacts on terahertz sensors.

1. Introduction

Recent interest in the terahertz region of the electromagnetic spectrum (arbitrarily defined as frequencies in the range 0.4 – 10 THz) has prompted development of imaging systems for this band in both the astronomical and terrestrial remote sensing communities. For the latter group, the advantage for sensors operating in the THz band is that they have the potential to combine the penetrating ability of radio frequency radiation with the sensitivity to chemical composition that is characteristic of infrared (IR) wavelengths. Thus, besides potential applications such as non-destructive screening of packages for hazardous materials, THz sensors can penetrate layers of clothing to detect contraband. These operating modes can, in many instances, involve indoor and outdoor operation over line-of-sight (LOS) distances of tens or hundreds of meters.

Unfortunately, THz band radiation (sometimes termed T-rays) is strongly absorbed by atmospheric water vapor, making it very sensitive to ambient absolute humidity, which restricts the range of practical detection for passive and (to a lesser degree) active THz sensors. Absorption and scattering of THz radiation may also be significant for heavy rain, snow, and fog, due to the large size of these atmospheric particulates relative to THz wavelengths (which are on the order of 0.5 mm).

Report Documentation Page				Form Approved OMB No. 0704-0188	
Public reporting burden for the collection of information is estimated to average 1 hour per response, including the time for reviewing instructions, searching existing data sources, gathering and maintaining the data needed, and completing and reviewing the collection of information. Send comments regarding this burden estimate or any other aspect of this collection of information, including suggestions for reducing this burden, to Washington Headquarters Services, Directorate for Information Operations and Reports, 1215 Jefferson Davis Highway, Suite 1204, Arlington VA 22202-4302. Respondents should be aware that notwithstanding any other provision of law, no person shall be subject to a penalty for failing to comply with a collection of information if it does not display a currently valid OMB control number.					
1. REPORT DATE 2006		2. REPORT TYPE		3. DATES COVERED 00-00-2006 to 00-00-2006	
4. TITLE AND SUBTITLE Modeling of Atmospheric Effects on Terahertz Imaging Systems				5a. CONTRACT NUMBER	
				5b. GRANT NUMBER	
				5c. PROGRAM ELEMENT NUMBER	
6. AUTHOR(S)				5d. PROJECT NUMBER	
				5e. TASK NUMBER	
				5f. WORK UNIT NUMBER	
7. PERFORMING ORGANIZATION NAME(S) AND ADDRESS(ES) U.S. Army Research Laboratory, Computational and Information Sciences Directorate, White Sands Missile Range, NM, 88002				8. PERFORMING ORGANIZATION REPORT NUMBER	
9. SPONSORING/MONITORING AGENCY NAME(S) AND ADDRESS(ES)				10. SPONSOR/MONITOR'S ACRONYM(S)	
				11. SPONSOR/MONITOR'S REPORT NUMBER(S)	
12. DISTRIBUTION/AVAILABILITY STATEMENT Approved for public release; distribution unlimited					
13. SUPPLEMENTARY NOTES ITEA Modeling and Simulation Conference, Dec 11-14, 2006, Las Cruces, NM					
14. ABSTRACT see report					
15. SUBJECT TERMS					
16. SECURITY CLASSIFICATION OF:			17. LIMITATION OF ABSTRACT Same as Report (SAR)	18. NUMBER OF PAGES 40	19a. NAME OF RESPONSIBLE PERSON
a. REPORT unclassified	b. ABSTRACT unclassified	c. THIS PAGE unclassified			

As part of the Defense Advanced Research Projects Agency (DARPA) funded effort, coordinated by the U.S. Army Night Vision and Electronic Sensors Directorate (NVESD), the U.S. Army Research Laboratory (ARL) Battlefield Environment Division is developing system performance and atmospheric effects models for generic THz sensors. In this paper, we shall discuss that portion of the ARL program concerned with the characterization of atmospheric effects upon prospective THz imaging systems.

2. General Simulation Approach

The basis of our image propagation approach involves simulation of a pinhole-type camera including an image plane, system lens, and objective field. Within this simulated space, pixels in the image plane are mapped as they pass through the object space until they reach a termination point in the external environment. This backward ray tracing method sums incremental path segment contributions for each ray to both the total atmospheric path radiance and the transmitted background scene radiance. The terminus of a ray trace occurs when the trace hits a target or background surface or the cumulative optical depth exceeds a very large preset value. Once this maximum value is reached, further significant incremental contributions to the cumulative path radiance are unexpected. This cutoff also avoids unnecessary computations for trace directions that traverse open atmosphere and will not intersect any solid target or background surface.

The model sensor (Figure 1) in the initial versions of our simulation was a simple large F-ratio camera of focal length f and with an $N \times N$ square array of uniformly-spaced pixels in its image plane. The physical length l of each side of the pixel array is specified by the user, as is the focal length f . The value of N is typically set to either 256 or 512 pixels, depending on run speed versus fidelity tradeoffs. Two types of targets are modeled: three-dimensional (3D) rectangular prism targets and billboard targets. The former target type has the advantage of being more physically realistic from the propagation standpoint, but it is of a simplistic structure. The latter class of targets can take actual THz short range imagery and simulate the appearance of these targets at longer ranges, with the disadvantage that the background radiances may be inaccurate, particularly if a passive billboard target is moved from an indoor to an outdoor situation.

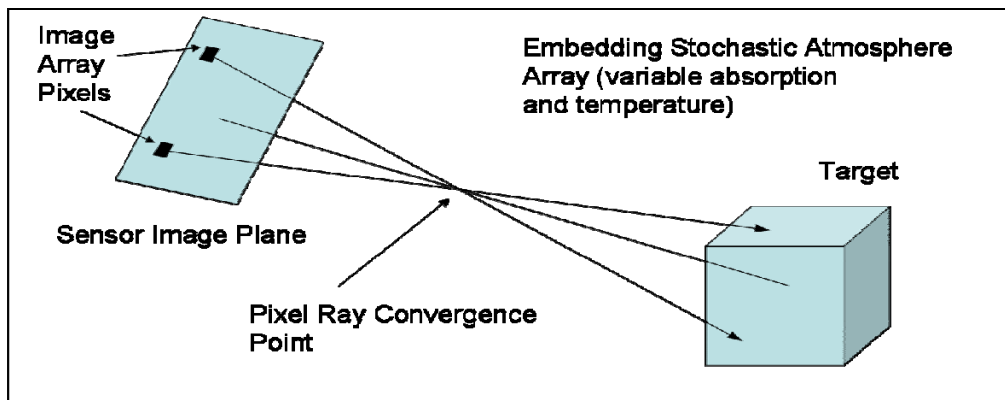


Figure 1. Schematic diagram of backward ray trace geometry.

The atmospheric environment through which the image ray tracing occurs is modeled as a 3D gridded space in which the amount of humidity varies from position to position in discontinuous increments via a system of volume elements (voxels). The length of each voxel is set by the user. Due to constraints of the computing environment, the voxel pattern is modeled using a $128 \times 128 \times 128$ periodic tiled cubical array.

3. Model Development

A crucial prerequisite for our THz image propagation model is an adequate statistical characterization of the water vapor density fluctuations observed in the atmosphere. We approached this problem through a series of field measurements using a fast hygrometer (model LI-7500, developed by LI-COR[®], Inc.) based on short-path transmissometry technology. This instrument was used to sense the advected water vapor concentration field at a 20 Hz sampling rate. Sonic anemometers located close to this sensor measured the wind speed and provided a means to convert measurements at discrete times into absolute humidity measurements at positions along a “wind run” axis. Figure 2 shows a sample of the data collected by an LI-7500 and a nearby sonic anemometer. Figure 3 shows these same data after conversion of the temporal axis to a spatial (wind run) axis, and rescaling of the water vapor concentration (in units of mmol m^{-3}) data into an absolute humidity measure (in units of g m^{-3}).

The field measurement data were then analyzed to produce a one-dimensional (1D) power spectrum of the absolute humidity fluctuations. After conversion of the time-series data for absolute humidity to the wind run format, a fast Fourier transform was applied to compute a 1D power spectrum for each one-hour batch of data. The spectra were fairly noisy, so a 5 point moving average was used to smooth them so that their structural form could be more readily compared to the known spectral behaviors of other conservative passive additive atmospheric properties (e.g., Kaimal et al., 1972). As expected, the spectra showed significant departures from power law behavior at very low and very high spatial frequencies, where source and dissipation phenomena should dominate, respectively.

The intermediate spatial frequencies (also known as the “inertial subrange”) did show conformity with a negative $5/3$ power law spectrum that is characteristic of a 1D Kolmogorov fluctuation spectrum. The 3D manifestation of this spectrum follows a negative $11/3$ power law form. Figure 4 illustrates the appearance of the raw and smoothed spectrum for the processed data of figures 2 and 3, along with a negative $5/3$ power law fit line.

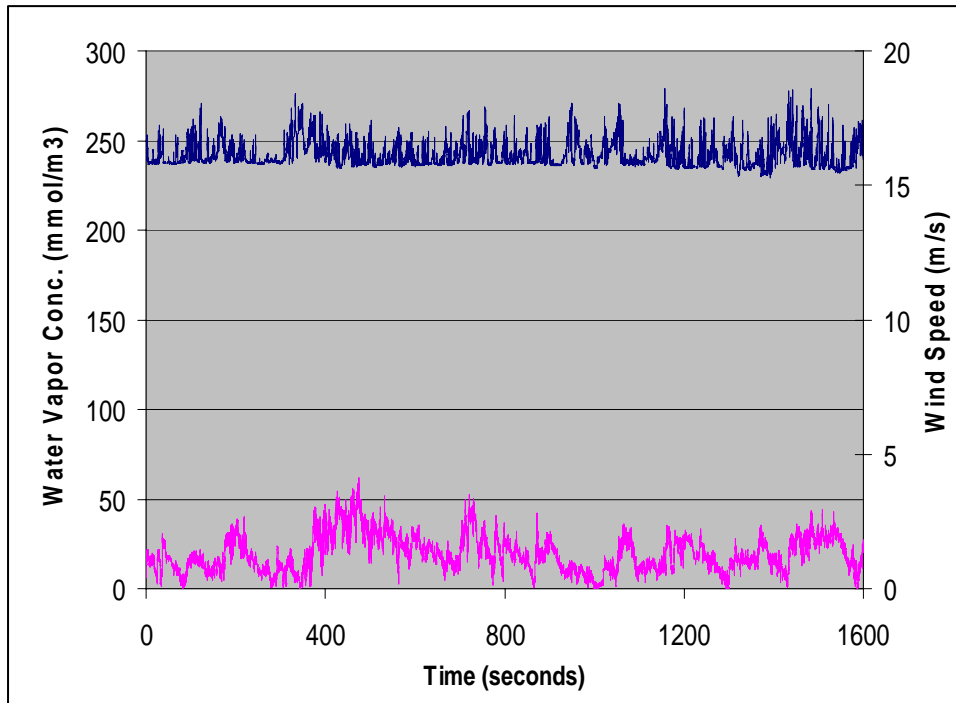


Figure 2. Water vapor concentration (upper curve) and horizontal wind speed (lower curve) measured for a 1600 s period starting at 1000 MST 27 March 2005 at White Sands Missile Range (WSMR), NM.

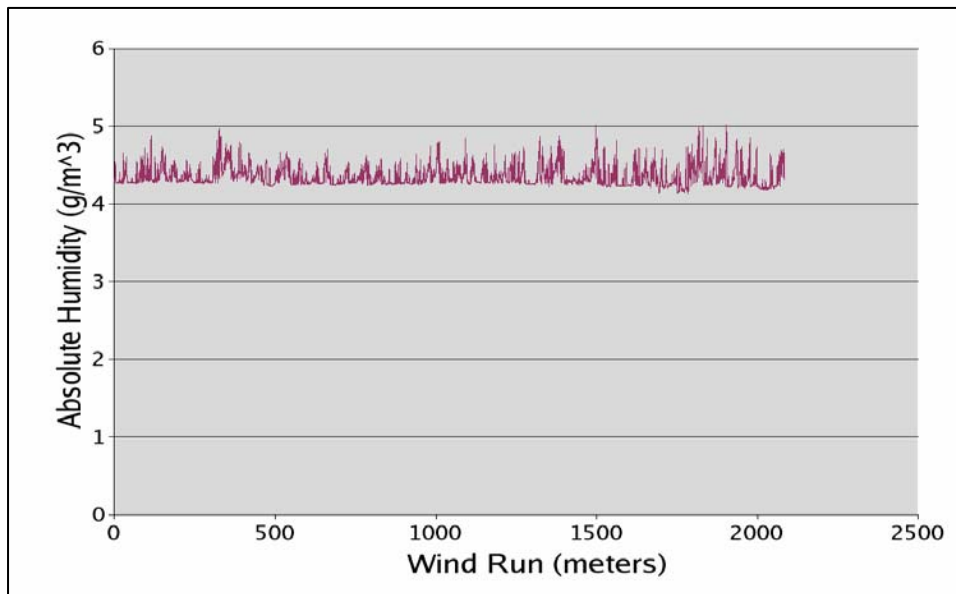


Figure 3. WSMR water vapor concentration data for 1000 MST 27 March 2005 after conversion to absolute humidity and wind run scaling.

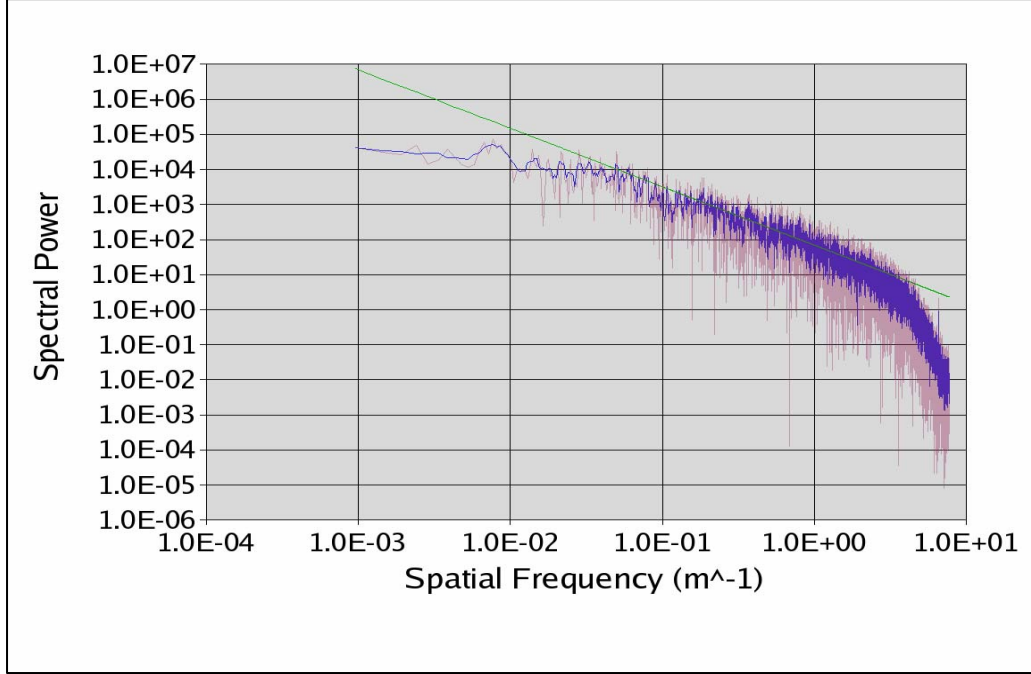


Figure 4. Spectral power density derived from water vapor concentration data measured over an hour period starting at 1000 MST 27 March 2005 at WSMR.

NOTE: The blue curve is the 5 point moving average. The green line is the negative 5/3 power law curve.

These power spectrum results are employed in our simulation to yield a stochastic (fluctuating) absolute humidity field $\rho_R(\mathbf{r})$ through the following relation (O'Brien and Tofsted, 2006):

$$\rho_R(\mathbf{r}) = \rho_0 \left[1 + \int \int \int_{-\infty}^{\infty} N_R(\xi) \Psi_\rho^{1/2}(\xi) \exp(i 2\pi \mathbf{r} \cdot \xi) d\xi \right], \quad (1)$$

where \mathbf{r} is the spatial position vector; ρ_0 is the spatial average of absolute humidity; ξ is the spatial frequency vector; $N_R(\xi)$ is a complex Gaussian random variate that has unit variance and a zero mean in both its real and complex parts; and $\Psi_\rho(\xi)$ is currently the negative 11/3 power law (Kolmogorov) 3D spectrum. The second term on the right hand side of equation (1) is the inverse 3D Fourier transform of the function $N_R(\xi) (\Psi_\rho(\xi))^{1/2}$. The square root arises from the 3D Fourier transform relationship between the power spectrum and the covariance of the absolute humidity fluctuations. When a Kolmogorov spectrum was fitted to and differenced with the observed spectral data (the zero mean), unit variance behavior was found to be a reasonable characterization for the inertial sub-range. The imaging model uses discrete formulations of the above expressions for $\Psi_\rho(\xi)$, $N_R(\xi)$, and $\rho_R(\mathbf{r})$, and a discrete FFT-based inverse transform (Tofsted, 2001).

Another critical component for our simulation is the 1993 version of the Millimeter-wave Propagation Model (MPM93) (Liebe et al., 1992 and 1993). This model enables us to convert the absolute humidity and temperature fields into a stochastic extinction coefficient field at various THz frequencies, which are used to directly compute ray trace radiances and transmissions in our imaging model. A typical MPM93 result for absorption coefficients spanning the 0.1 to 1 THz frequency band is shown in Figure 5. Our imaging model

encapsulates MPM93 results over a wide range of frequencies, atmospheric temperatures, and relative humidities in the form of a look-up table (LUT) that is interpolated to provide THz extinction coefficients for arbitrary absolute humidity, temperature, and frequency.

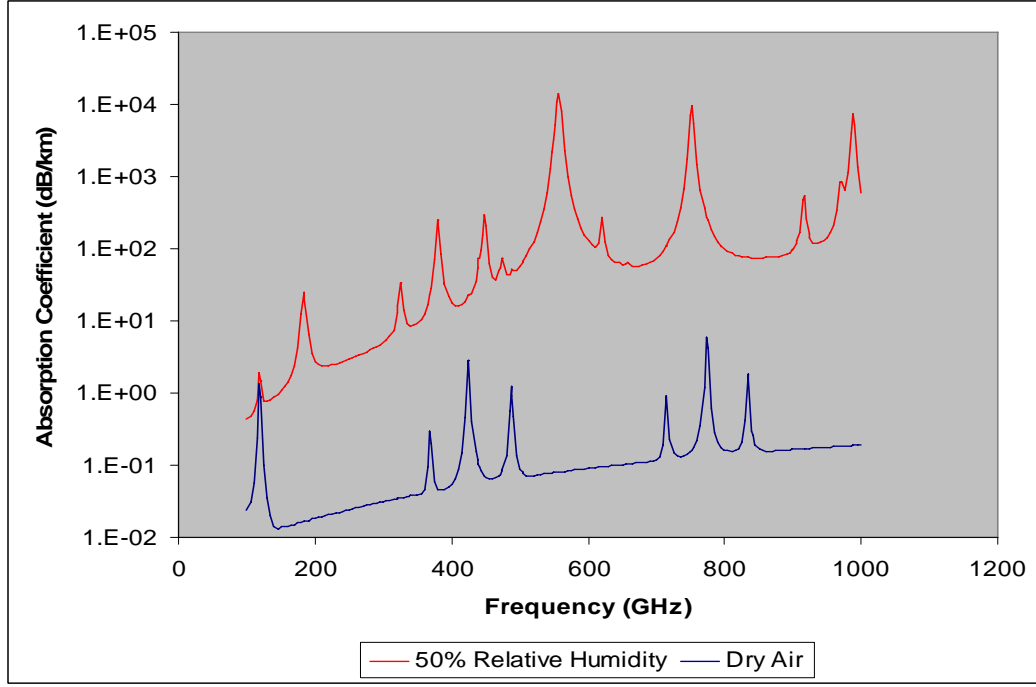


Figure 5. Comparison of MPM93 absorption coefficients for moist (50% relative humidity) and dry (0% relative humidity) air at 15 °C and 1 atmosphere.

Once a stochastic absolute humidity field has been computed through application of equation (1) and the MPM93 model, the model proceeds to ray trace from each pixel position in the image plane back to object points in the external environment. For passive calculations, where no active THz sources illuminate the target, the total spectral radiance $L(s)$ for an LOS path of length s is the sum of the attenuated target radiance and incremental path radiance over a path of N segments (Hoock et al., 1992; O'Brien and Tofsted, 1998 and 2006):

$$L(s) \cong L_T(s) \exp\left(-\sum_{j=1}^N \bar{K}_j \Delta s_j\right) + \sum_{i=1}^N \exp\left(-\sum_{j=0}^{i-1} \bar{K}_j \Delta s_j\right) \left[1 - \exp(-\bar{K}_i \Delta s_i)\right] \bar{L}_{s_i}, \quad (2)$$

where $L_T(s)$ is the unattenuated target radiance; K_i and Δs_i are the respective extinction coefficient and length of line segment i ; and \bar{L}_{s_i} is the limiting path radiance. The limiting path radiance is the radiance that would result as the optical depth of the medium tends to large values. If scattering is neglected (which is a good approximation in the THz band in the absence of heavy rain, snow, or fog), the limiting path radiance is essentially the blackbody radiance at ambient atmospheric temperature. Our imaging model currently follows this assumption, since it does not yet incorporate THz hydrometeor scattering algorithms.

Three variants of our imaging model exist to handle different sensing modes: 1) spectral (single frequency) passive, 2) broadband passive, and 3) active. The spectral and broadband modes use equation (2) to calculate pixel radiances. The broadband mode sums over frequency bins weighted by sensor response and includes sensor sensitivity via a noise equivalent power (NEP) input. Thus, even with contrast stretching, sensor noise will limit the target contrast once the attenuated target signal falls below a threshold level. Examples of this phenomenon will be seen in section 4. The active mode assumes that a narrow band source illuminates the target and that only the first term of equation (2), multiplied by an outgoing transmission factor, is a significant contributor to the apparent pixel radiance. This assumption is motivated by the fact that even modest active THz sources have enormous effective blackbody temperatures in the THz region. For the active imaging examples shown below, we used the nominal source characteristics for the active source used by the Ohio State University (OSU) group in laboratory imaging, which had an effective source brightness temperature of 10^{18} K.

4. Results

We first exercised the passive spectral radiance version of our model for 3D targets with uniform or simple periodic surface emissivities. Figure 6 illustrates how the appearance of a rectangular box target might vary as its surface temperature under fixed atmospheric conditions. We have used MPM93 results to establish a mean value for the extinction at a study frequency of 650 GHz. As can be seen from figure 5, 650 GHz is a frequency where water vapor extinction is near a local minimum or “window.” The results shown in figure 6 use the Kolmogorov spectrum for fluctuations about this mean, as implemented from equation (1). The ground plane is at a temperature of 273 K, the atmospheric mean temperature is 275 K, and both the box and ground plane are assigned reflectivities of 0.2. A vertical bar pattern is imposed on one of the target box faces, with bar temperatures alternating between the nominal target value and that of the ground plane.

The target temperature is depressed 10 K below the ground plane temperature in figure 6(a) and displays strong negative contrast in the contrast-stretched image. The same holds true for figure 6(b), where the target temperature is depressed by 5 K, although some lightening is evident on the target sides and bar pattern. The target is at the same temperature as the ground plane in figure 6(c), as evidenced by the disappearance of the ground temperature/target temperature bar pattern and the indistinctness of the edges of the target that rest on the ground plane. However, strong negative contrast is visible on all of the elevated target edges due to absorption and emission from the background atmosphere. Figures 6(d) and 6(e) represent a 1 K and 2 K elevation of target temperature above that of the ground plane. As one might expect, some vertical target edge regions begin to show positive contrast, but the upper target edges still display appreciable negative contrast. Only with the target temperature elevated 5 K over the ground plane temperature and 3 K above the atmospheric temperature do we finally see near zero contrast on the upper edges, as seen in figure 6(f).

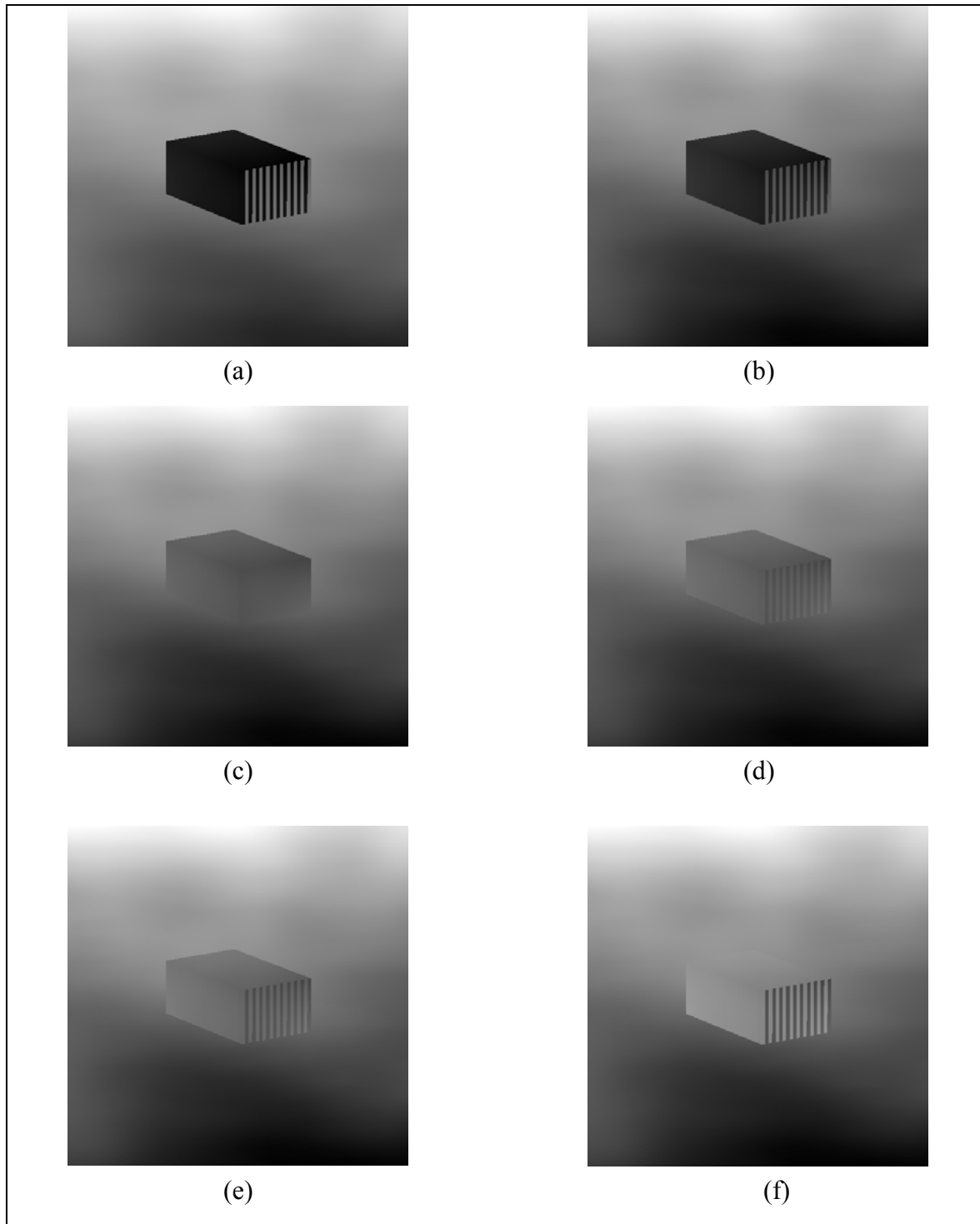


Figure 6. Variation of 650 GHz target contrast with target temperature in a Kolmogorov spectrum emission/absorption atmosphere. Target temperatures were (a) 263 K, (b) 268 K, (c) 273 K, (d) 274 K, (e) 275 K, and (f) 278 K. Ground and air temperatures were 273 K and 275 K respectively.

Next, we considered a more realistic sensor that incorporated operational properties of passive scanned bolometric sensors similar to those designed by the TIFT team at OSU. We assumed a nominal passband of 100 GHz centered at a frequency of 650 GHz and integrated in 25 GHz steps. The 0.3 m aperture sensor had a frame rate of 100 Hz and a detector NEP of $3 \times 10^{-12} \text{ W Hz}^{-1/2}$, yielding a noise power of $3 \times 10^{-11} \text{ W}$. The random additive pixel noise in the detector was then computed as the noise power multiplied by a Gaussian random number variate of zero mean and unity standard deviation. This noise component was applied to ray traces over a 60×60 pixel image plane for a billboard target that is a THz image of a subject with a mock-up pistol concealed beneath a layer of clothing. The results of the simulation are displayed in figure 7 for two different propagation ranges (40 m and 80 m) and four levels of average absolute humidity (0.7, 7.6, 17.9, and 35.7 g m^{-3}). The results clearly demonstrate some of the shortcomings of the passive imaging mode. At 80 m, all of the images have severe noise degradation of the signal, even for the relatively cold and dry scenario on the left-hand column of the figure. The 40 m cases show reasonable performance up to absolute humidities in the neighborhood of 7.6 g m^{-3} , but noise effects are still quite apparent even at low humidities.

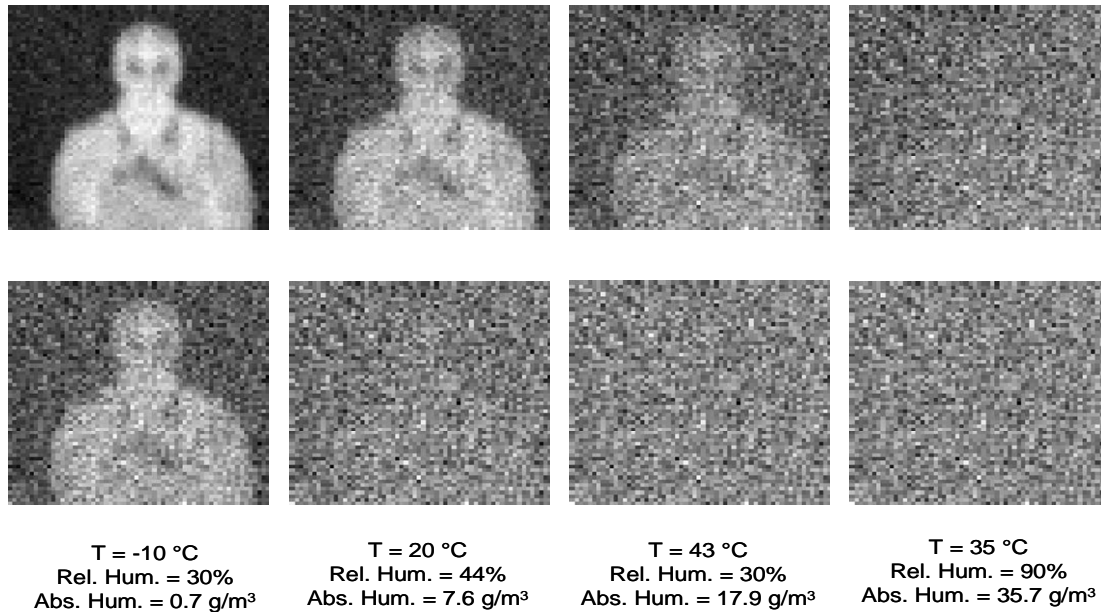


Figure 7. Broadband passive imaging examples centered at 650 GHz. Images in the upper row are at a range of 40 m, those in the bottom row are at 80 m.

The OSU group also has developed short range active THz systems. Figures 8 and 9 show results for a simulated propagated active mode image at 650 GHz, for sensor dynamic ranges R (maximum detectable radiance divided by minimum detectable radiance) of 80 and 50 dB, with a threshold minimum detectable power $L_0 = 10^{-3} \times 10^{-R/10} \text{ W}$. The source power was assumed to be 1 mW for the examples shown here, which use the same set of path lengths and atmospheric conditions as the passive cases above.

80 dB Dynamic Range

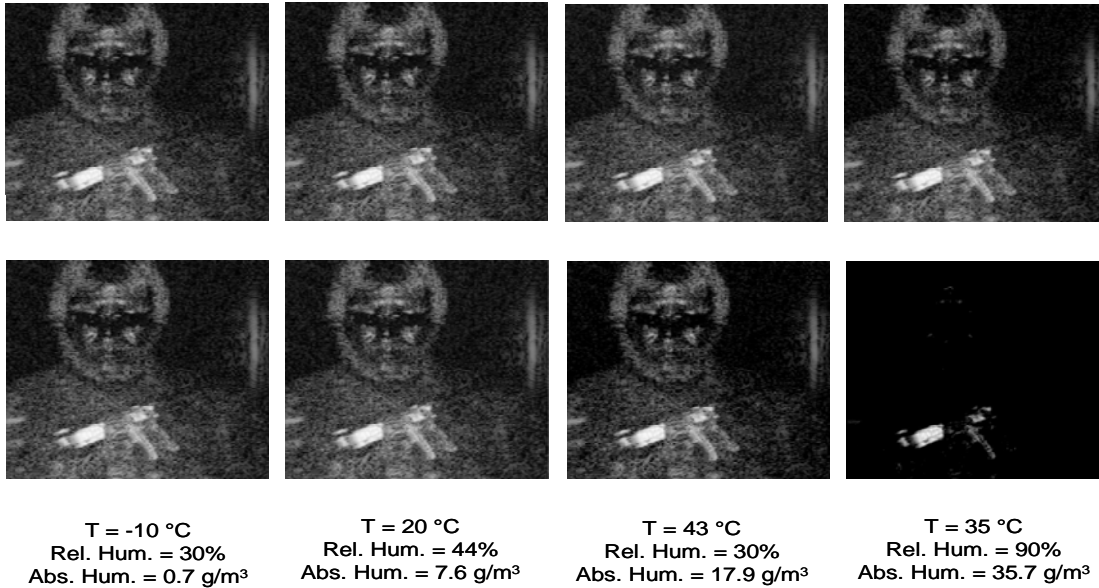


Figure 8. Active imaging example for 650 GHz source. The dynamic range of sensor was set to 80 dB. The top row is at a range of 40 m, the bottom row is at 80 m.

50 dB Dynamic Range

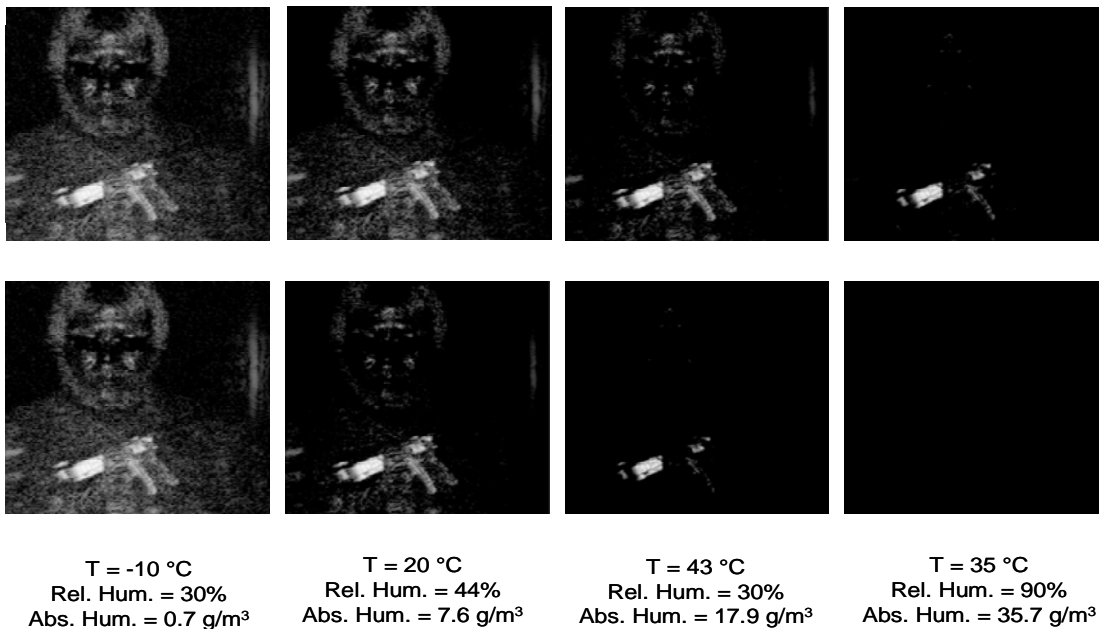


Figure 9. Active imaging example for 650 GHz source. The dynamic range of sensor was set to 50 dB. The top row is at a range of 40 m, the bottom row is at 80 m.

The active imaging mode shows much better performance than does the passive mode through equivalent atmospheric conditions. With an 80 dB sensor dynamic range, target features are significantly degraded only at the longest range and highest absolute humidity. The imaging performance degrades at considerably lower absolute humidities for the 50 dB case, however.

5. Conclusions and Future Work

The THz imaging model described in this paper shows promise as a means to investigate atmospheric impacts on both real and potential imaging systems. However, there are several areas where the package must be significantly improved before this capability becomes a reality. First, the characterization of the geometrical, optical, and thermal properties of the 3D environment must be made more complete. Existing target models employed by target acquisition packages need to be investigated as resources that might satisfy part of this requirement. Another significant part of the THz environmental description task might be addressed by studies of natural and manmade background surface emissivity and thermal characteristics in the millimeter wave literature.

We will also need to improve the sensor model to incorporate the more detailed real world properties of optical and electronic systems that we know will significantly impact performance. In particular, we will need to apply a modulation transfer function (MTF) methodology to the image formation process. The engineering models that characterize these imperfections of the sensor system are well known, but as yet we do not have well defined real-world THz system designs to which they may be applied. Differences in image appearance will also depend on the scanning technique used. Instantaneous scanning of all pixels produces one result. Single-pixel scanning allows the humidity field to evolve during the image acquisition process, etc.

If hydrometeors are present in the atmosphere for operational scenarios, it will also be very important to add a hydrometeor scattering-absorption algorithm to the active source model. Liebe's MPM93 (or a similar) model provides the absorption component for snow and rain attenuation of the source beam, but it does not directly supply any estimate for the scattered radiance. This effect could significantly modify the path radiance signal. In the absence of such resonance-scale objects as snow crystals or rain drops, the atmospheric water vapor will simply attenuate the illumination beam. The terahertz reflectance properties for target and background surfaces will also be critical scenario elements.

References

- Hoock, D.W., Giever, J.C., O'Brien, S.G. & Burlbaw, E.J. (1992). *A multi-stream radiative transfer model for inhomogeneous, three-dimensional aerosol clouds*. Proceedings of the 1992 Battlefield Atmospherics Conference, U.S. Army Research Laboratory, White Sands Missile Range, NM.
- Kaimal, J.C., Wyngaard, J.C., Izumi, Y. & Cot'e, O.R. (1972). *Spectral characteristics of surface-layer turbulence*. Q. J. Roy. Met. Soc. 98, 563–589.
- Liebe, H.J., Hufford, G.A. & Cotton, M.G. (1992). *Progress in atmospheric propagation modeling at frequencies below 1000 GHz*. Proceedings of the 1992 Battlefield Atmospherics Conference, Fort Bliss, Texas.

Liebe, H.J., Hufford, G.A. & Cotton, M.G. (1993). *Propagation modeling of moist air and suspended water/ice particles at frequencies below 1000 GHz*. Proceedings of AGARD 52nd Specialists' Meeting of the Electromagnetic Wave Propagation Panel, Palma de Mallorca, Spain.

O'Brien, S.G. & Tofsted, D.H. (2006). *Development of a terahertz short range imaging model*. Proceedings of SPIE, Vol. 6239.

O'Brien, S.G. & Tofsted, D.H. (1998). *Physics-based visualization of dense natural clouds. II. Cloud-rendering algorithm*. Appl. Opt. 37, No. 33, pp. 7680-7688.

Tofsted, D.H. (2001). *Turbulence Simulation: On Phase and Deflector Screen Generation*. ARL-TR-1886, U.S. Army Research Laboratory, White Sands Missile Range, NM 88002.

Acknowledgements

The authors wish to thank the Dr. Mark Rosker of the DARPA TIFT program office, Dr. Richard Espinola of NVESD, Dr. Frank DeLucia of OSU, Dr. Eddie Jacobs of Memphis State U. (formerly of NVESD), and Messrs. Jimmy Yarbrough, David Quintis, and Manuel Bustillos of ARL for their funding, programmatic, and field support of this work.



Modeling of Atmospheric Effects on Terahertz Imaging Systems

Sean O'Brien

David Tofsted

U.S. Army Research Laboratory

Computational and Information Sciences Directorate

White Sands Missile Range, NM 88002



Introduction - I

- Key Background Points:
 - Recent advances in terahertz imaging sensor technology are leading to higher frame rates and pixel density
 - Some terahertz sensor applications will involve outdoor operation in various climatic environments
 - Atmospheric absorption is strong in the low terahertz band (0.5 – 1 GHz), and is due primarily to water vapor



Introduction - II

- Issues for Outdoor Terahertz Operation:
 - Statistics for spatial variation of water vapor mass density (or absolute humidity) about the mean are poorly known, particularly as functions of terrain and prevailing weather conditions
 - Functional form for the spectral power density of absolute humidity is not well known
 - Target contrast as a function of range for terahertz active and passive imagers is not well established



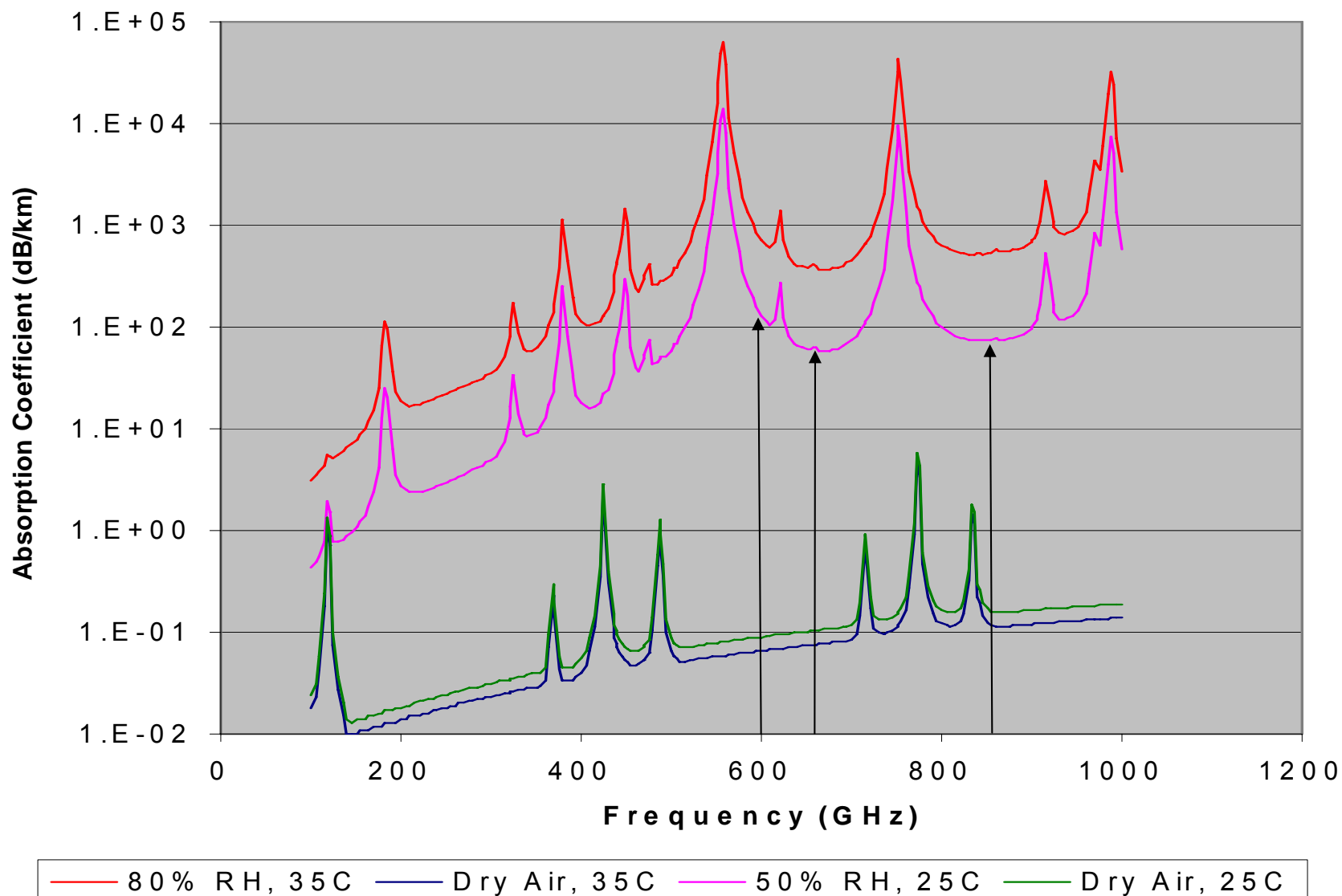
Introduction - III

- Simulation Approach:
 - Collect preliminary water vapor fluctuation field data and create analysis methods and software
 - Analyze absolute humidity data to establish reasonable functional shape for spectrum and amplitude for fluctuations
 - Use readily available models to connect simulated stochastic absolute humidity and air temperature fields with absorption and radiance fields at terahertz frequencies
 - Implement a ray-trace imaging model for billboard and three-dimensional targets in the simulated stochastic atmosphere



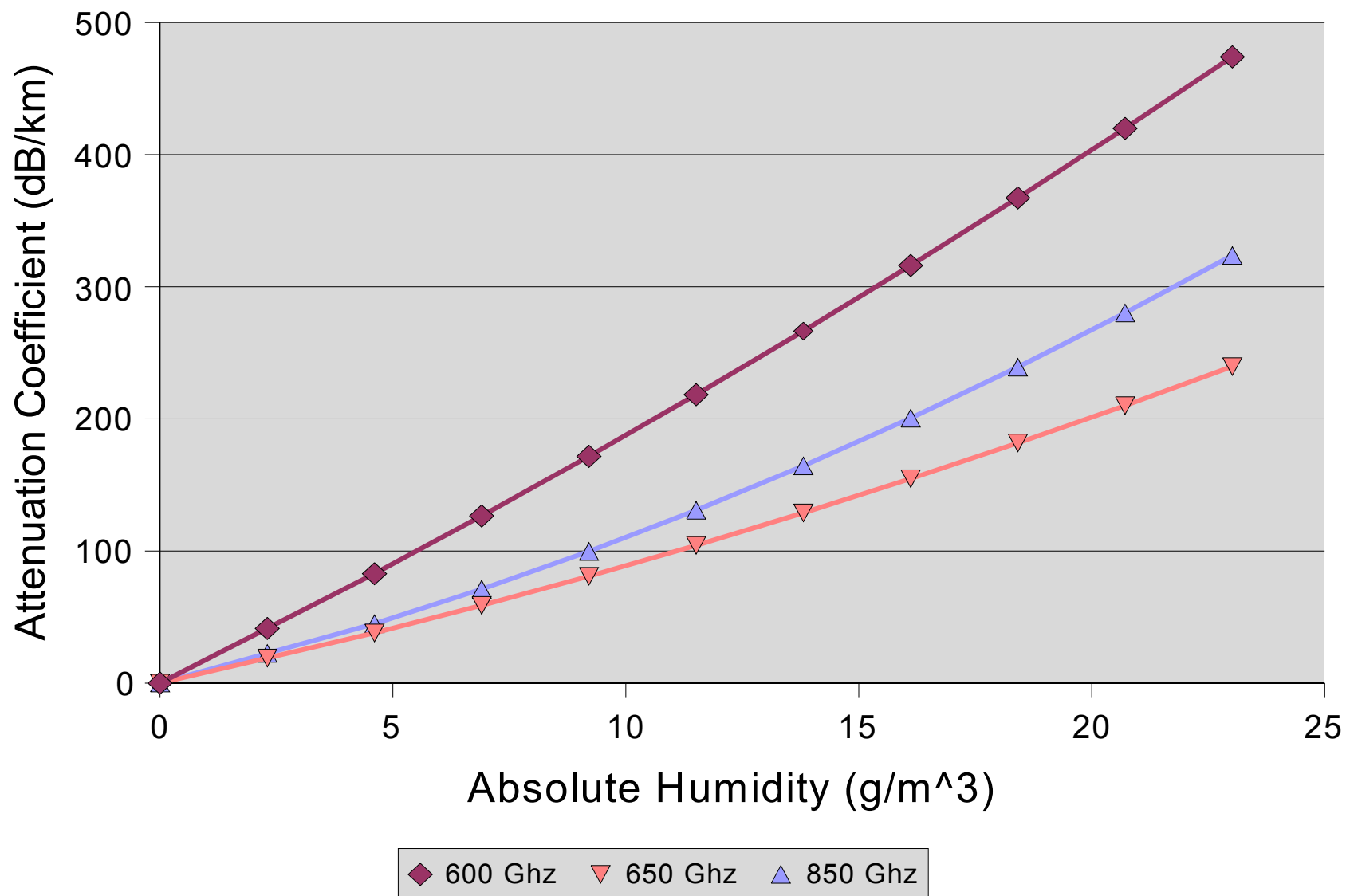
MPM93 Absorption Coefficient

Results: $T_{\text{Atm}} = 25\text{C}, 35\text{C}$



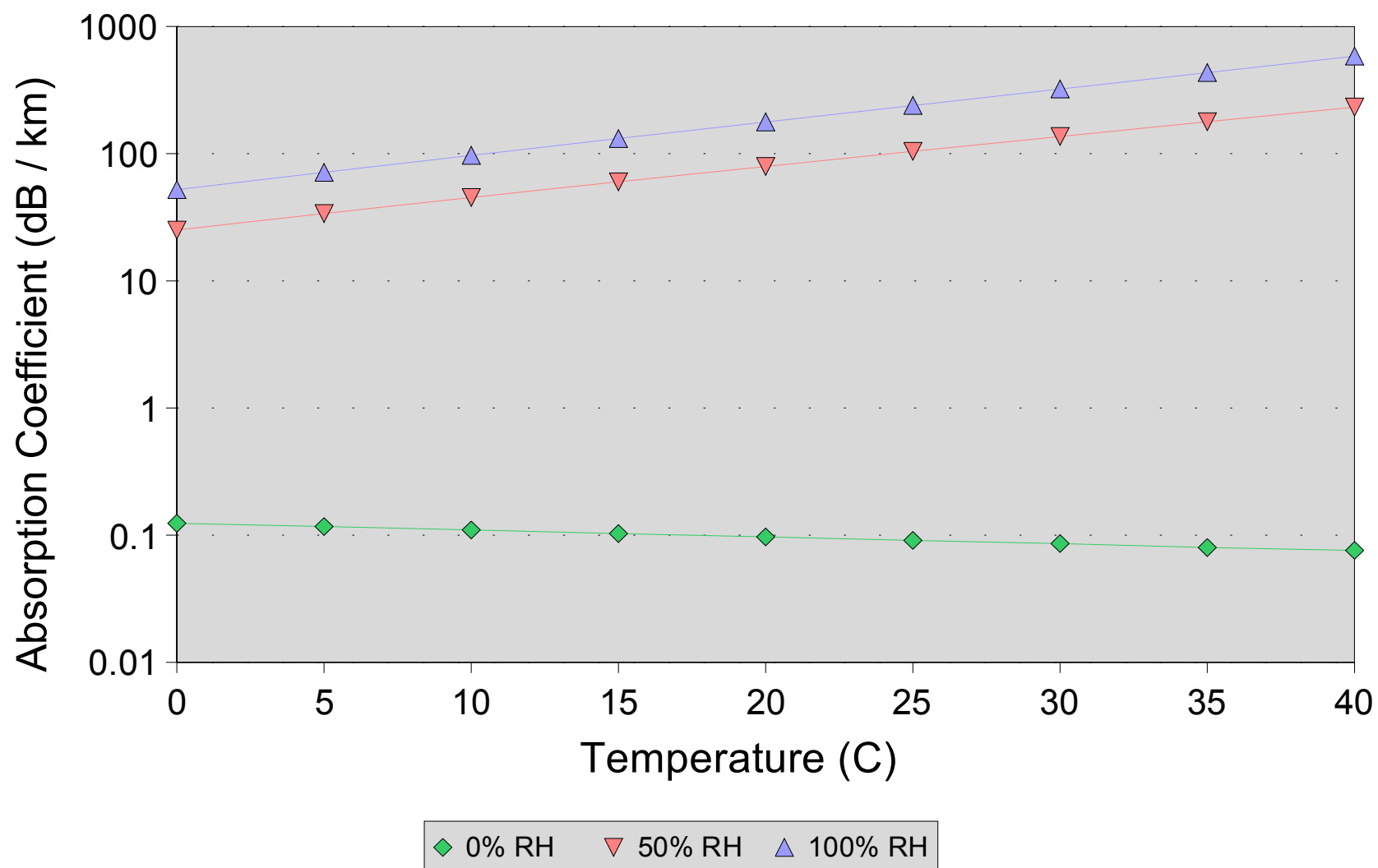


MPM93 Sample Results: 25 °C





MPM93 Sample Results: 650 GHz



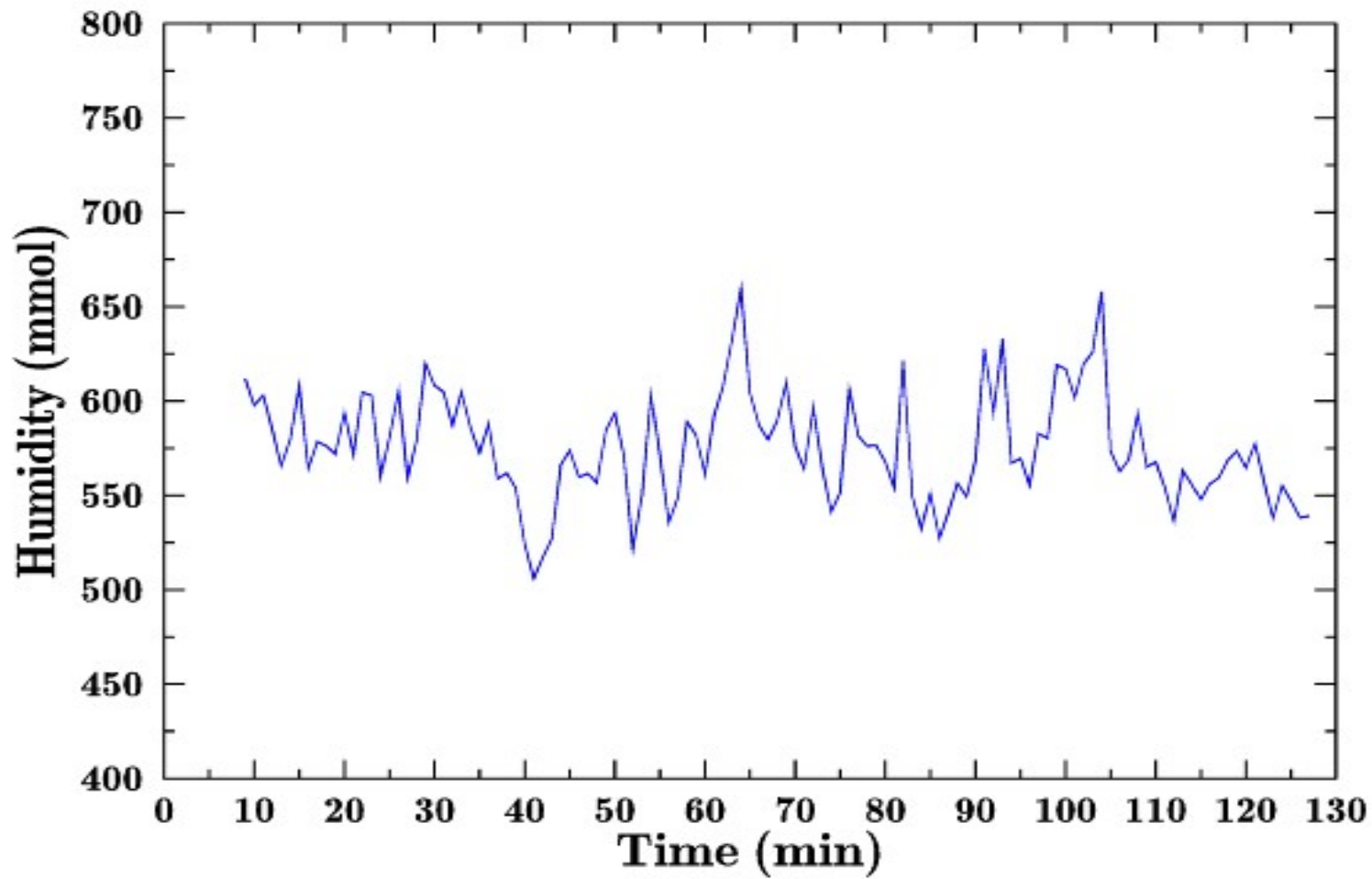


WSMR Water Vapor Measurements

- Measurement Periods: 23-28 Mar 05, late Aug 05
- Measurement Sampling
 - 20 Hz rate
 - 1 hour data batches
 - Continuous over day
- Measurement Apparatus
 - Single Li-Cor Model LI-7500 absolute humidity sensor system
 - Four sonic anemometer probes and support equipment

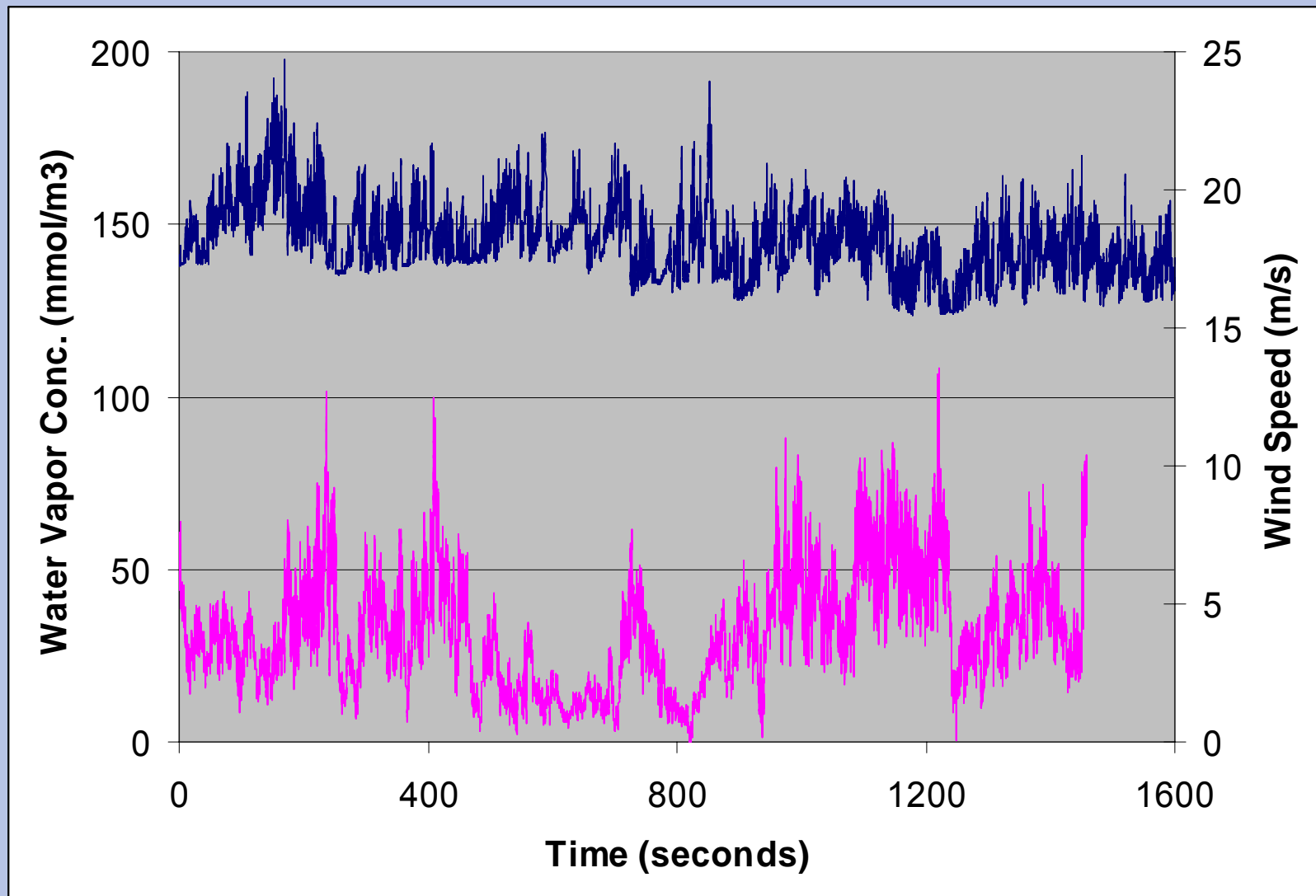


Example from August 05 Las Cruces Measurements



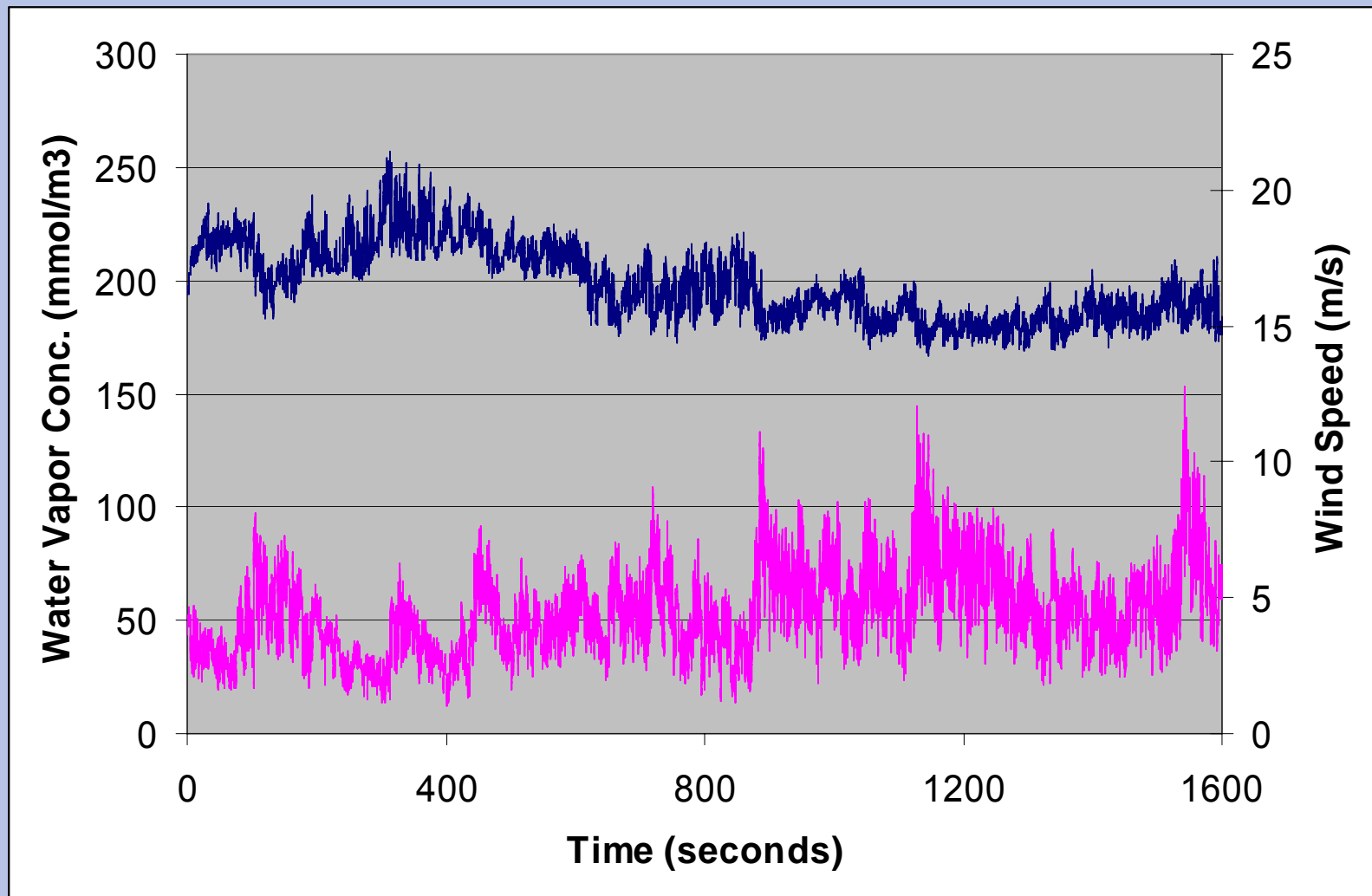


WSMR Water Vapor Measurement Results: 23 Mar 05 1600 MST





WSMR Water Vapor Measurement Results: 26 Mar 05 1000 MST

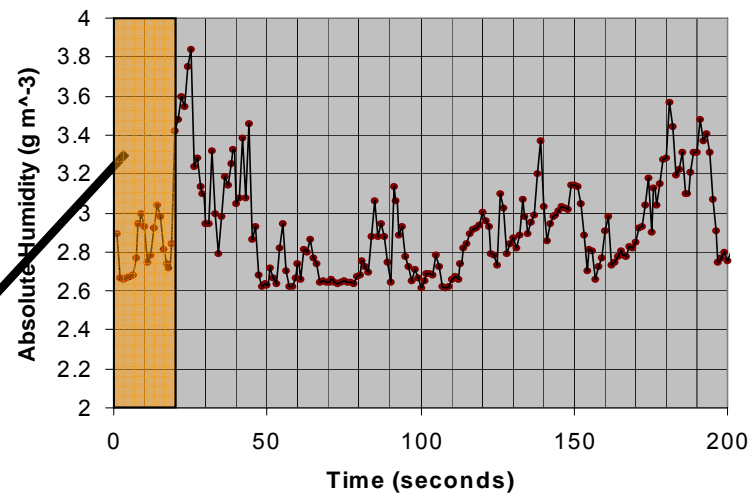




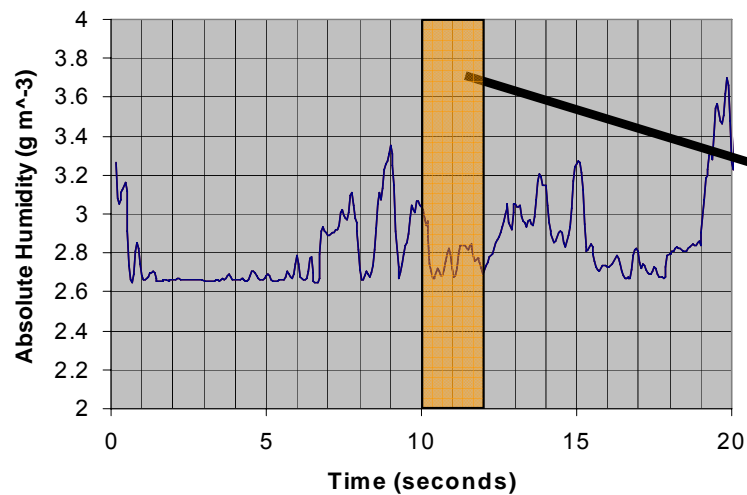
Absolute Humidity Variations on Different Time Scales



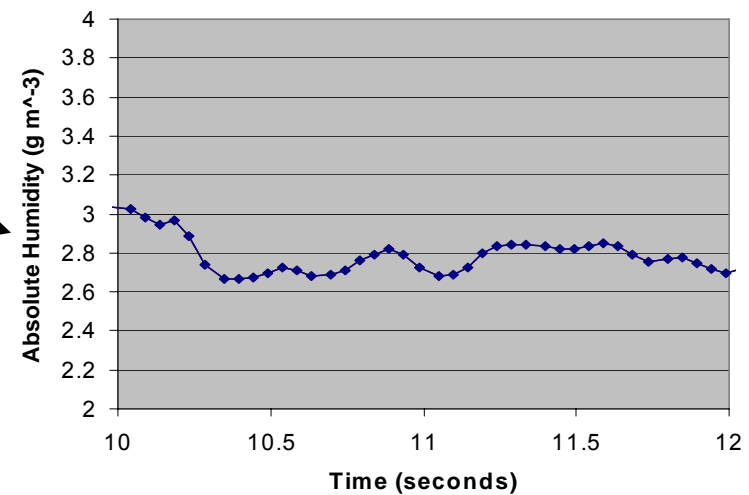
1 Second Averages of 20 Hz Data



20 Hz Data Sampling Rate

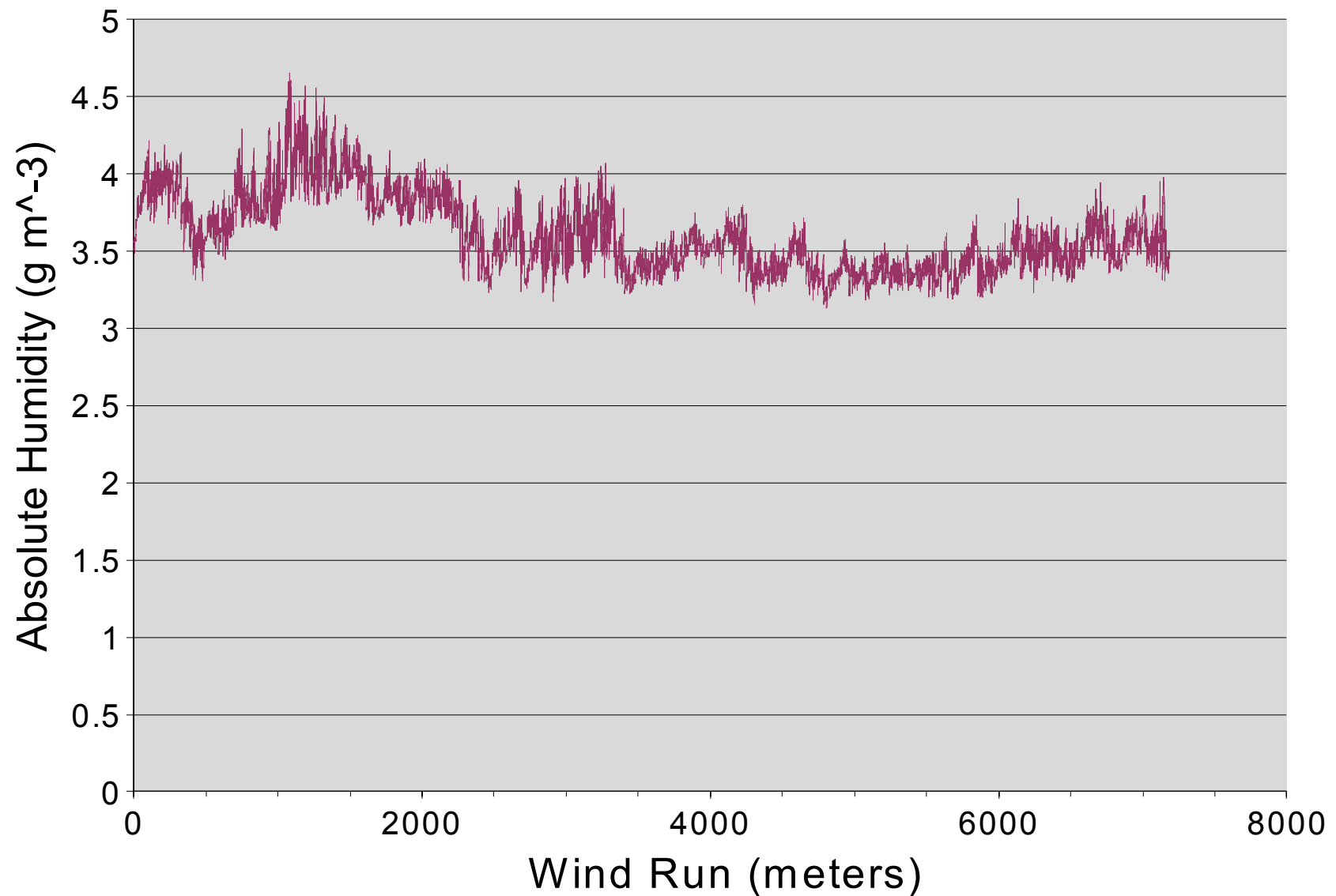


20 Hz Data Sampling Rate





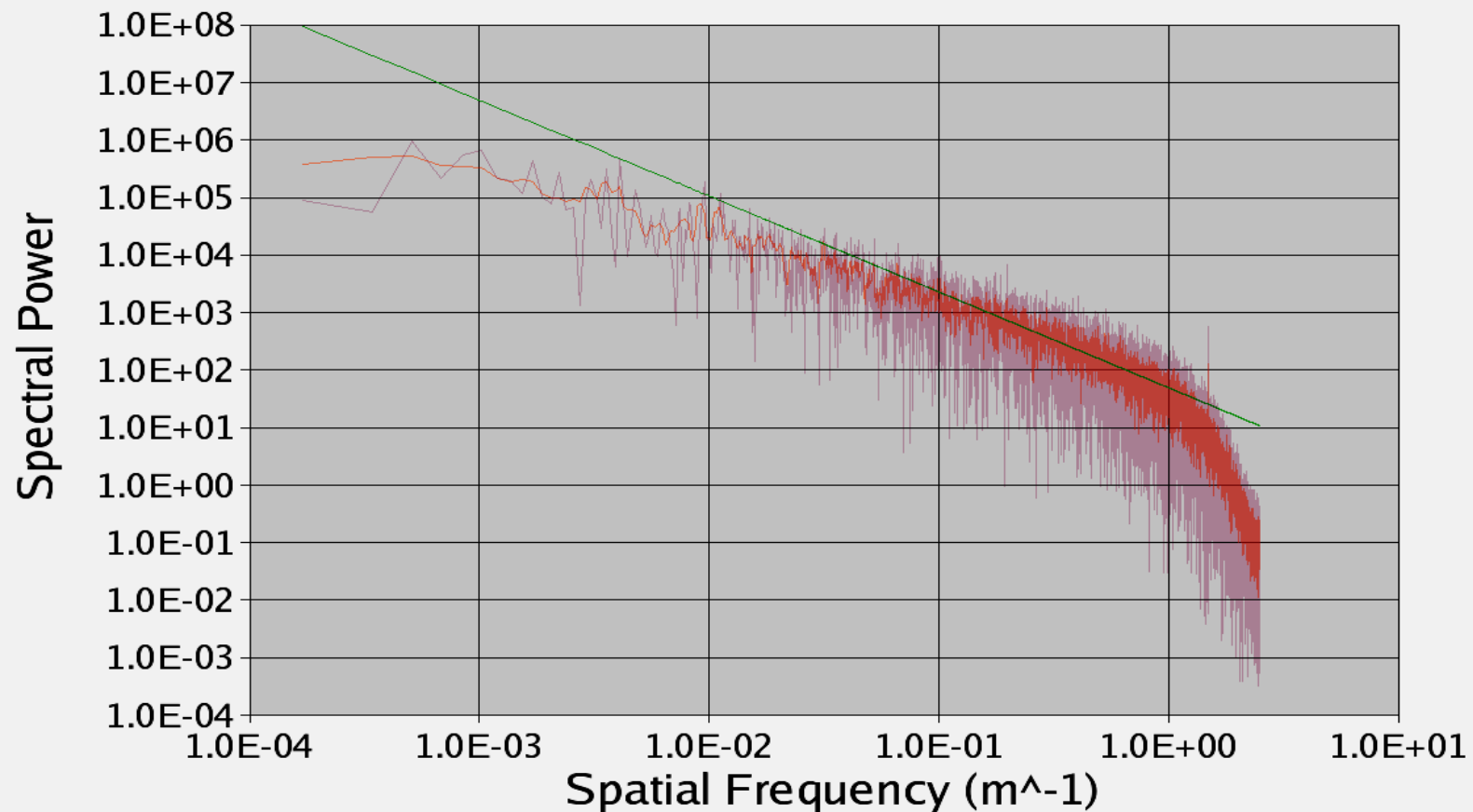
WSMR Water Vapor Measurement Results: 26 Mar 05 1000 MST





Absolute Humidity Spectrum

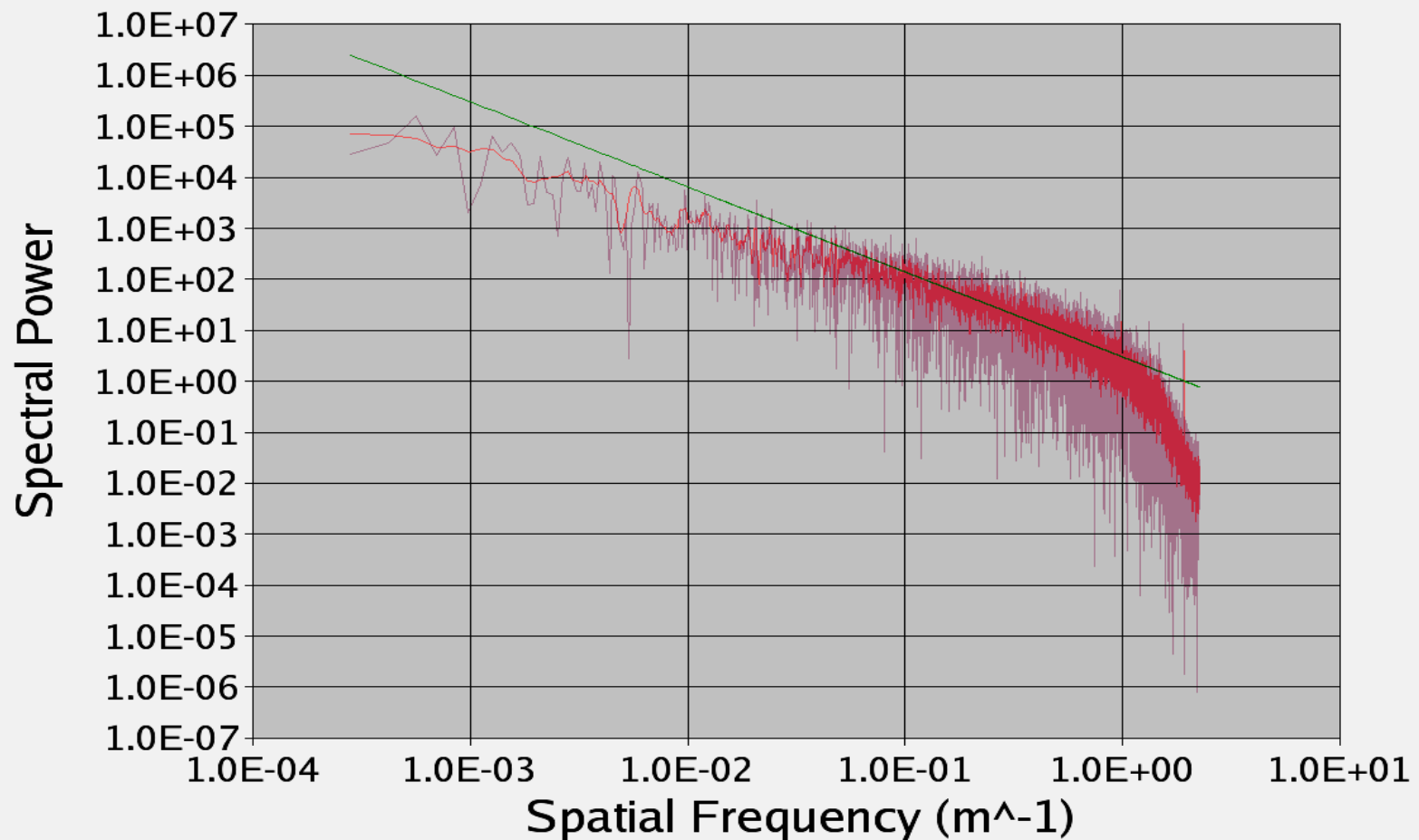
23 Mar 05 1600 MST





Absolute Humidity Spectrum

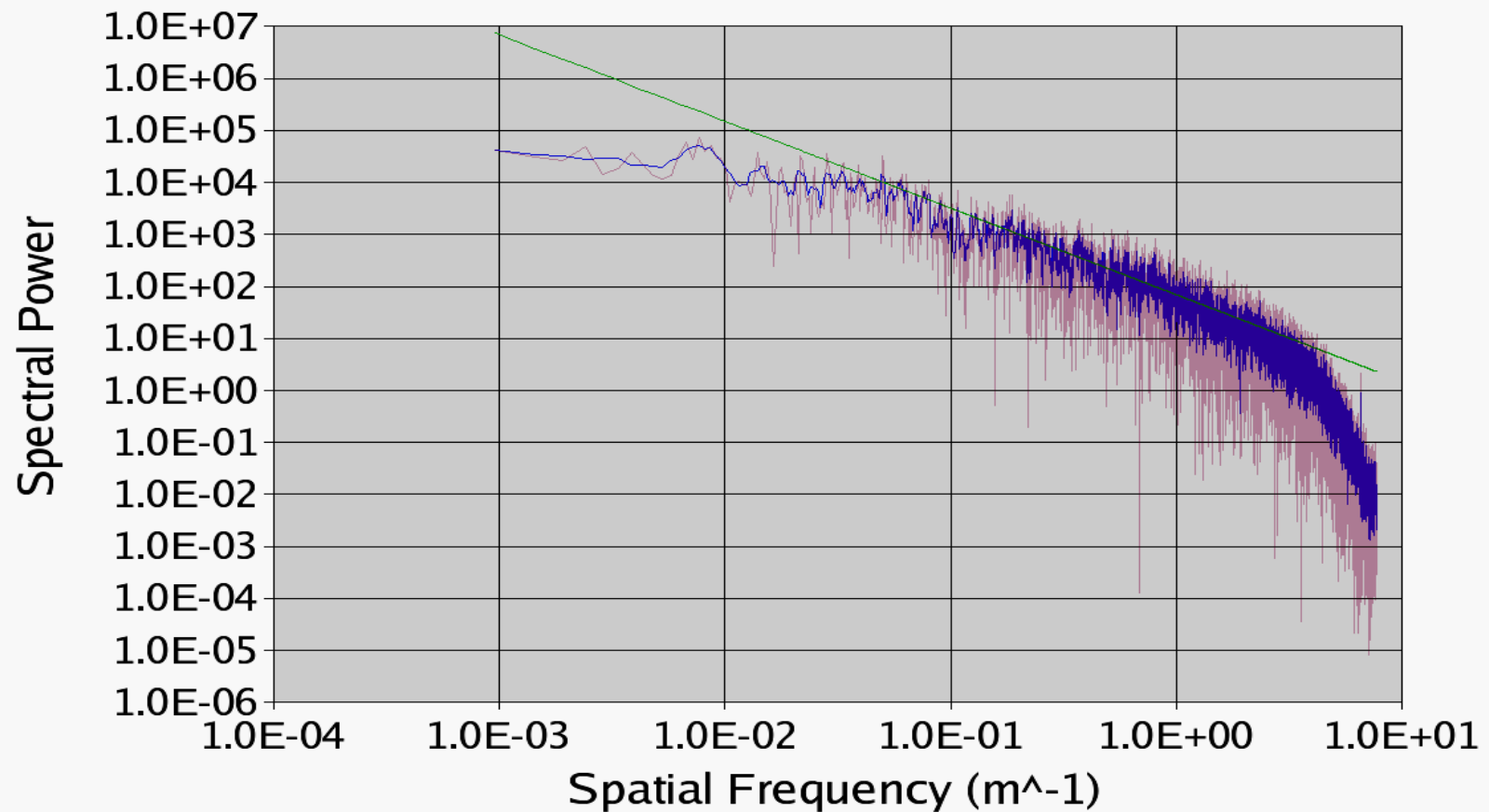
26 Mar 05 1700 MST





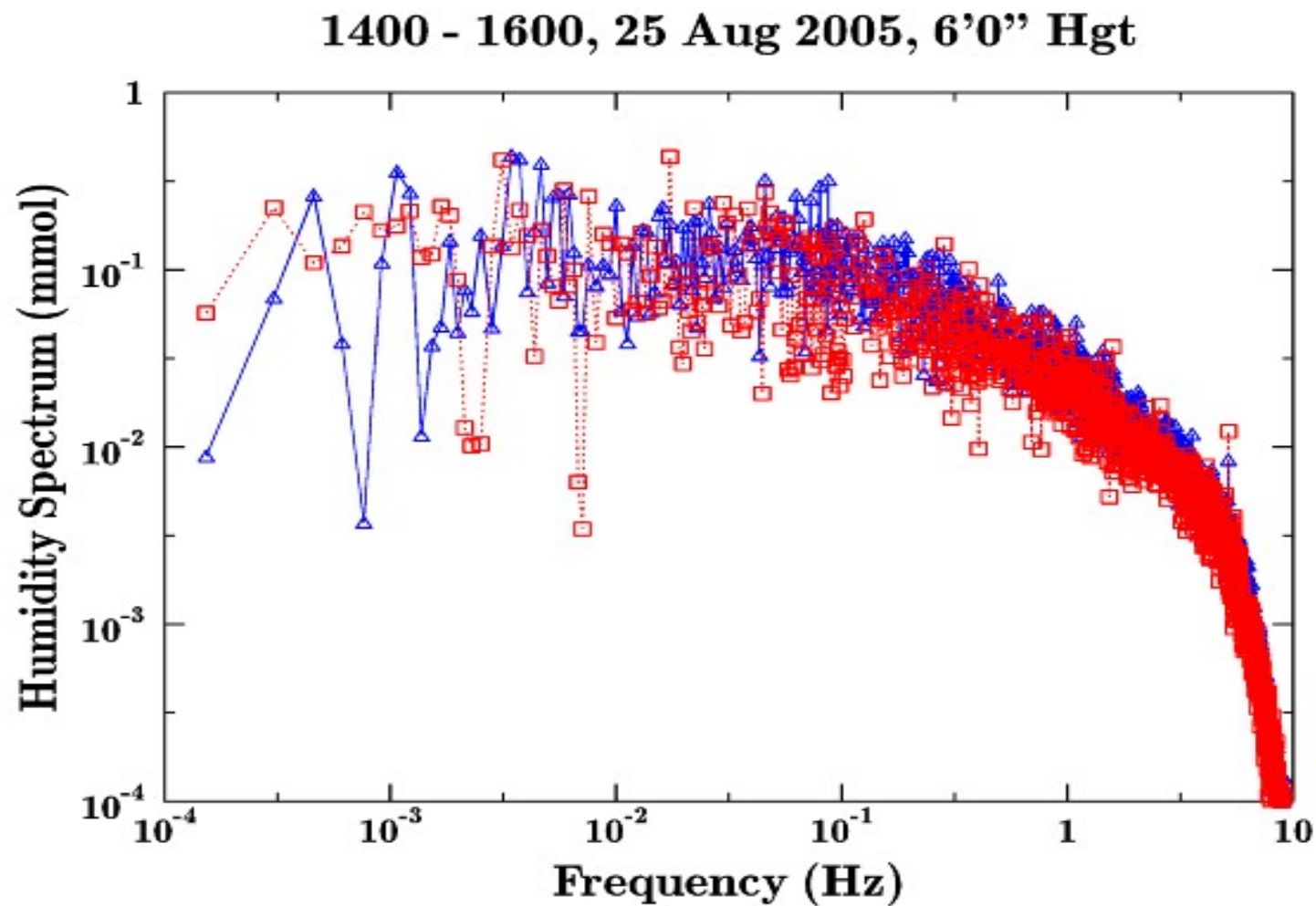
Absolute Humidity Spectrum

27 Mar 05 1000 MST



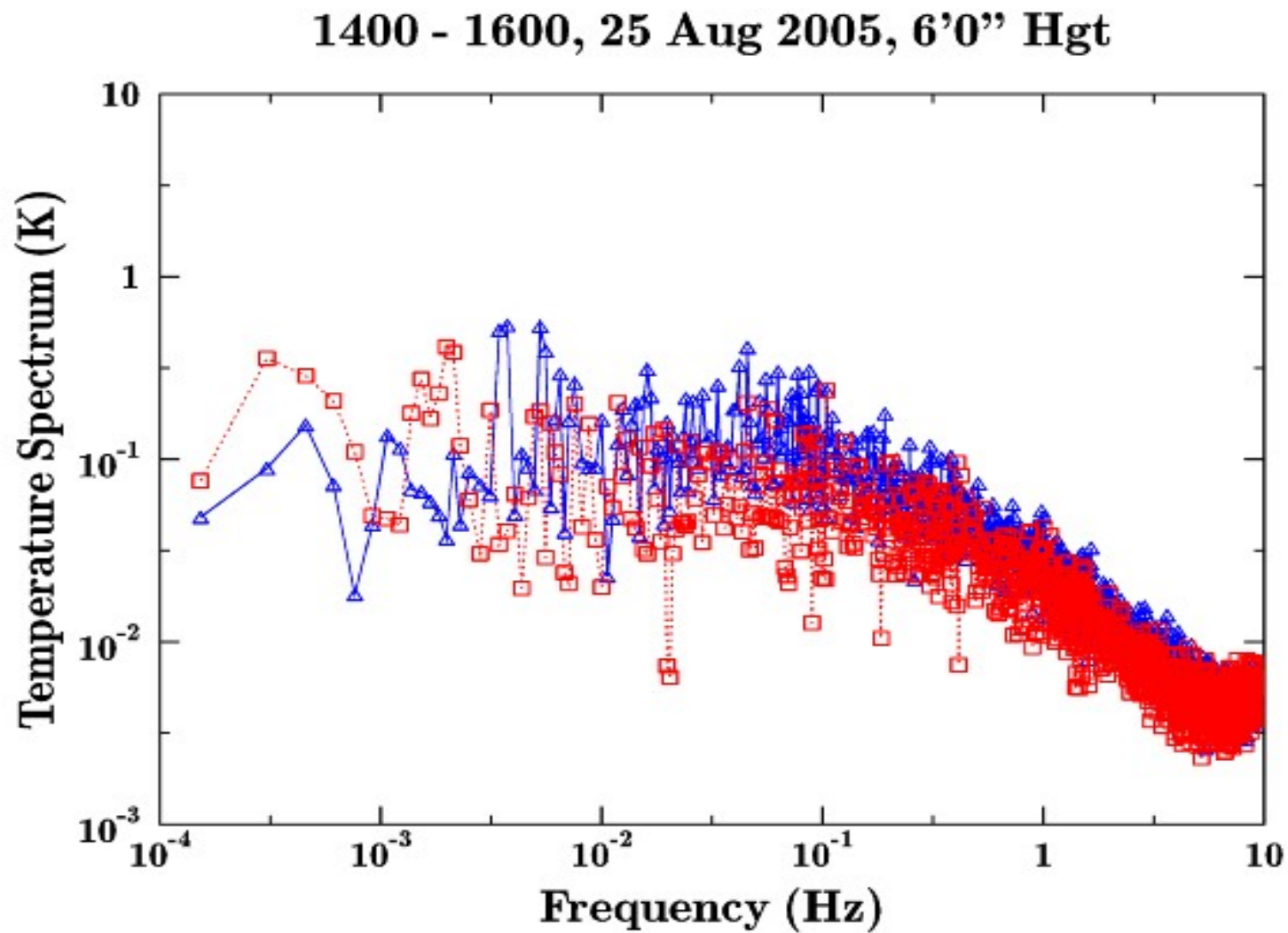


Higher Absolute Humidity Example





Temperature Spectrum Example





Simulation of Atmospheric Fluctuations



- The one-dimensional distribution of absolute humidity $\rho(x)$ may be expressed as the sum of an average $\rho_0(x)$ and a randomly fluctuating component $\rho_1(x)$:

$$\rho(x) = \rho_0(x) + \rho_1(x)$$

- The randomly fluctuating component has an expectation value of zero:

$$\langle \rho_1(x) \rangle = 0$$

- Under the assumption that the spatial expectations and spatial averages are equivalent (homogeneity), the correlation of ρ values at two different locations x_1 and x_2 may be expressed using the covariance function

$$\Gamma_\rho(x_1, x_2) = \langle [\rho(x_1) - \langle \rho(x_1) \rangle] [\rho(x_2) - \langle \rho(x_2) \rangle] \rangle ,$$

or

$$\Gamma_\rho(x) = \langle \rho_1(x_1) \rho_1(x_1 + x) \rangle$$



Simulation of Atmospheric Fluctuations



- A three-dimensional covariance value for the random fluctuation ρ_R may then be defined by

$$\Gamma_{KR}(\mathbf{r}) = \int \int \int_{-\infty}^{\infty} N_R(\xi) \Psi_K(\xi) e^{i2\pi\mathbf{r}\cdot\xi} d\xi$$

- This result is then be used to define an expression for the random fluctuation field about a mean value:

$$\rho_R(\mathbf{r}) = \rho_0 + \int \int \int_{-\infty}^{\infty} N_R(\xi) \Psi_K^{1/2}(\xi) e^{i2\pi\mathbf{r}\cdot\xi} d\xi$$

where the three-dimensional Kolmogorov inertial sub-range spectrum with integration constant C is given by

$$\Psi(\xi) = C \xi^{-11/3}$$

with the spectrum and covariance related by the transform pair

$$\Psi_K(\xi) = \int \int \int_{-\infty}^{\infty} \Gamma_K(\mathbf{r}) e^{-i2\pi\mathbf{r}\cdot\xi} d\mathbf{r}$$

$$\Gamma_K(\mathbf{r}) = \int \int \int_{-\infty}^{\infty} \Psi_K(\xi) e^{i2\pi\mathbf{r}\cdot\xi} d\xi$$



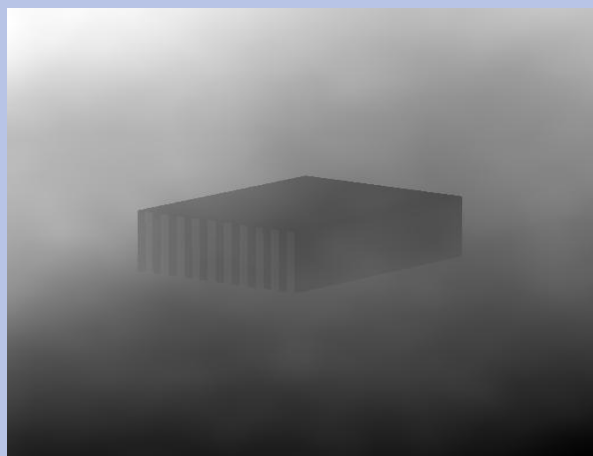
Synthetic Image Example



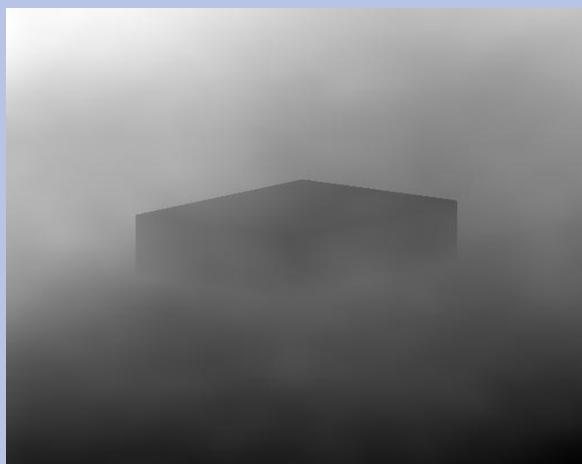
- 650 GHz, albedo = 0.2 for target and ground
- 2 m x 1.5 m x 0.6 m box target
- -X face of target has alternating $T_{\text{GND}}/T_{\text{TGT}}$ vertical stripes
- Sensor at $(x,y,z) = (0, 0, 15 \text{ m})$
- Target at $(50 \text{ m}, 40 \text{ m}, 0.3 \text{ m})$
- Sensor focal length 150 mm, 10 mm square focal plane, 512 x 512 pixels
- T_{ATM} , T_{GND} fixed at 288 K (15 °C), 285 K
- 100% RH, Kolmogorov spectrum, 20% σ



3D Target at 650 GHz,
 $T_{\text{ATM}} = 288 \text{ K}$, $T_{\text{GND}} = 285 \text{ K}$, T_{TGT} Varied



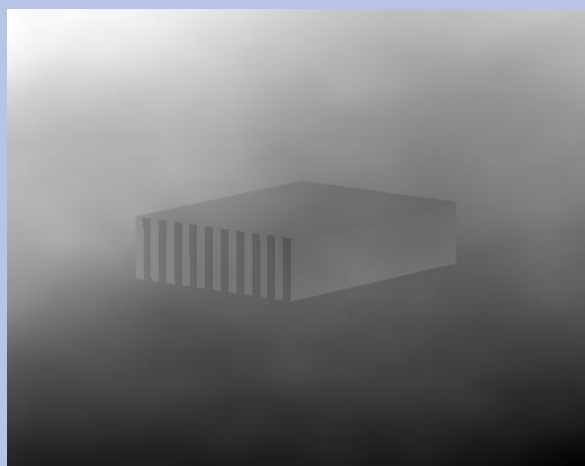
284 K



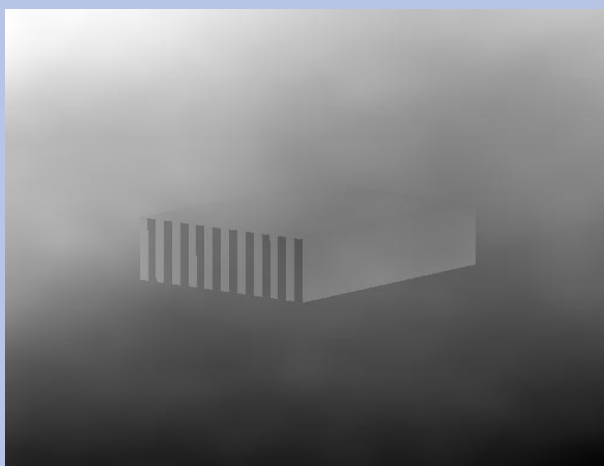
285 K



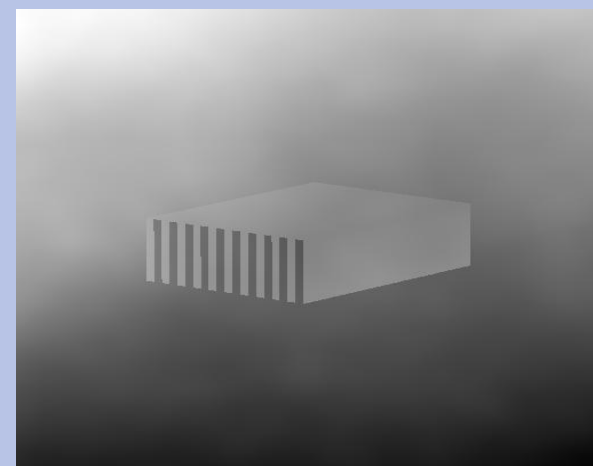
286 K



288 K



290 K



292 K



Planned Terahertz Atmospheric Imaging Model Upgrades

- Active imaging
 - Bistatic and monostatic options
- Hydrometeor treatment
 - Rain and snow absorption and scattering
- Simplified user input
 - Relative humidity instead of absolute humidity
 - Option for user input of temperature and humidity variances
- More choices for sensor performance characteristics
 - Focal plane array or raster scan image formation methods
 - More realistic system noise and angular resolution properties
- Obtain better terahertz band background imagery data as it becomes available



Planned Field Support Work

- Continue analysis of WSMR/Las Cruces Li-Cor and sonic anemometer data
- Collect and analyze WSMR data sets using two Li-Cor sensors at variable spacings to get absolute humidity covariance
- Collect and analyze concurrent Li-Cor and sonic anemometer data sets to determine cross variance between temperature and absolute humidity



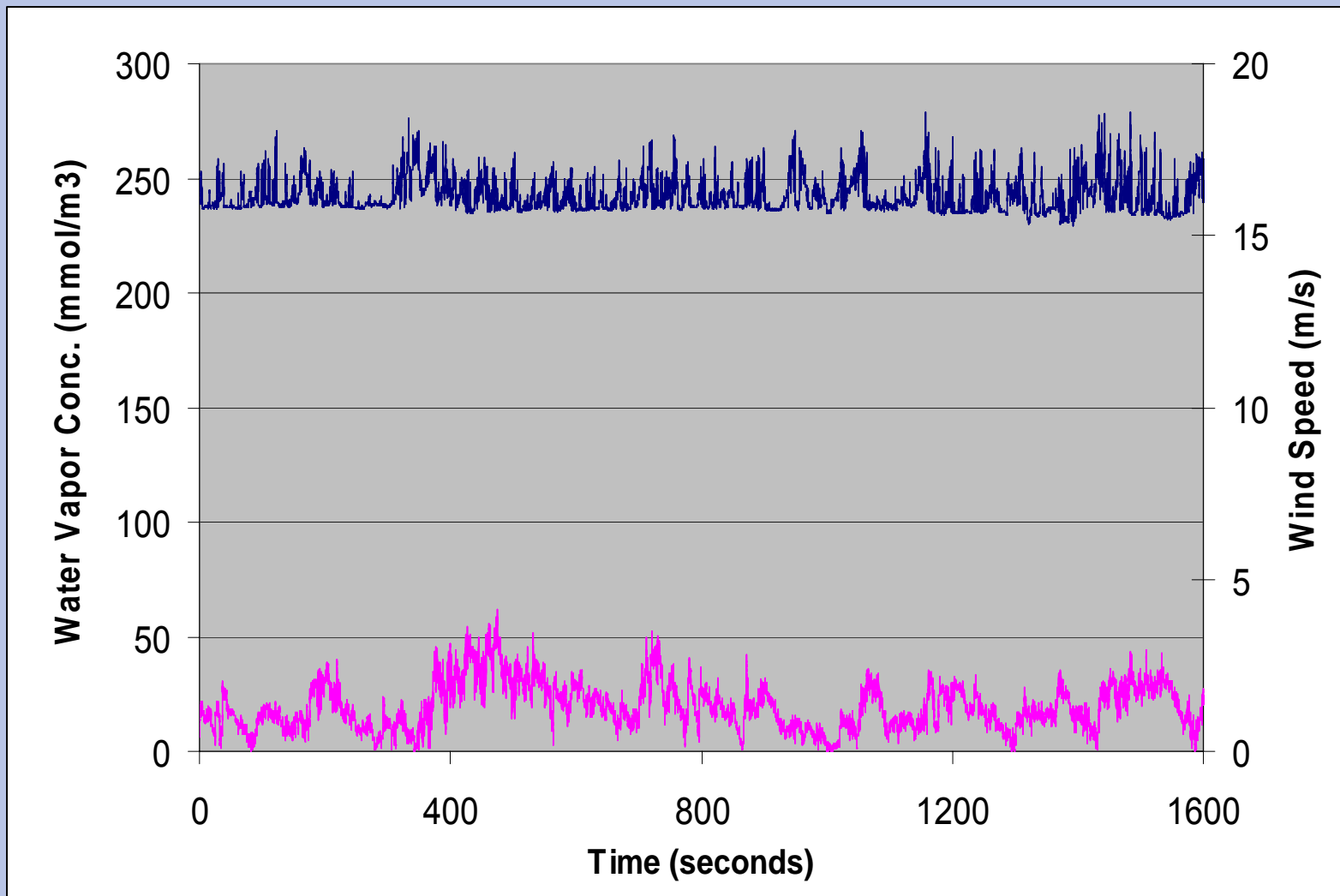
Supplementary Slides





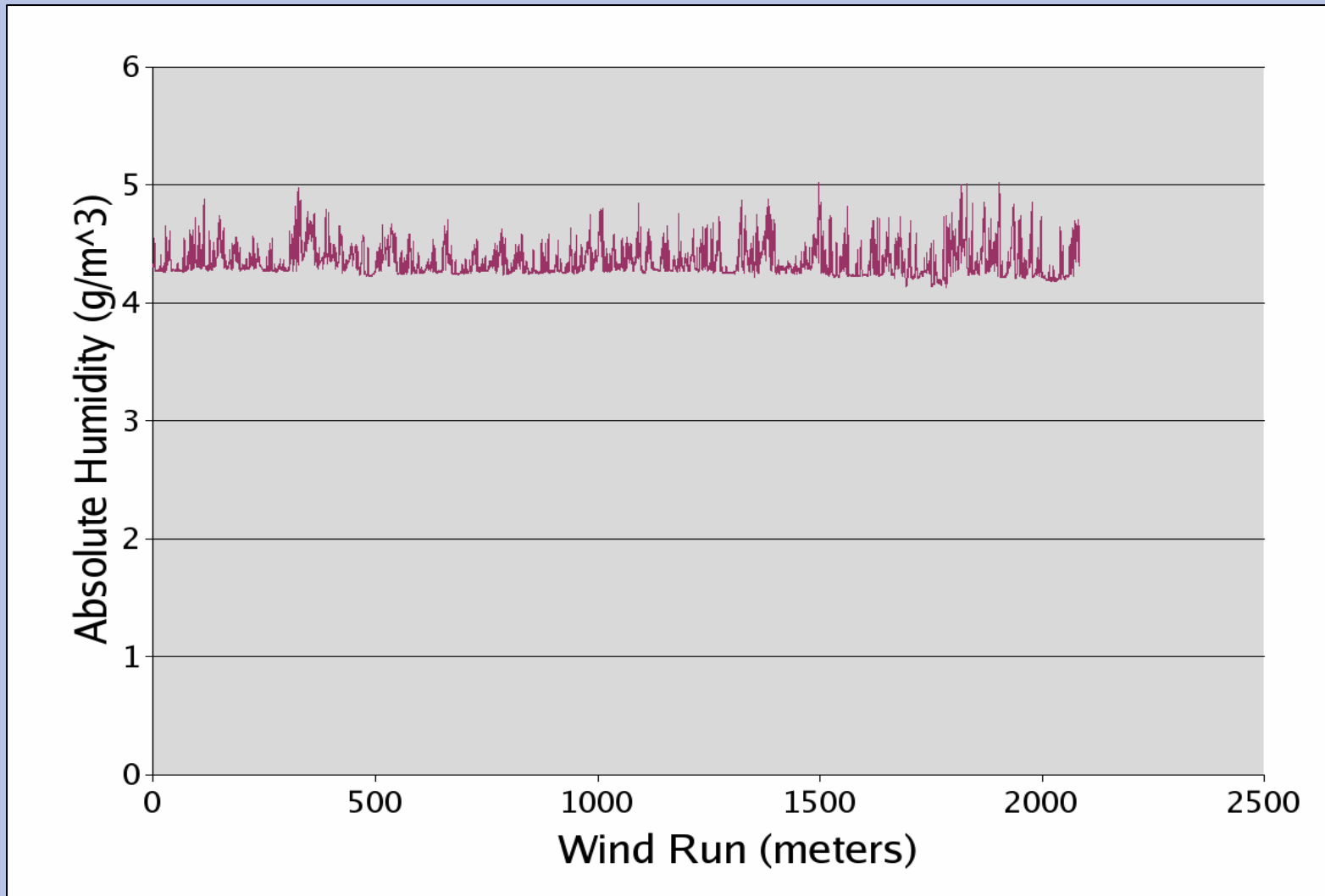
WSMR Water Vapor Measurement

Results: 27 Mar 05 1000 MST





WSMR Water Vapor Measurement Results: 27 Mar 05 1000 MST





MPM93 Sample Results: $T = 25^{\circ}\text{C}$, Frequency = 600 GHz

Rel. Hum. (%)	Vapor Press. (mb)	Abs. Hum. (ρ) (g / m ³)	Attenuation (dB / km)	Abs. Coeff. (m ⁻¹)	$\Delta K/\Delta \rho$ (m ² / g)
0	0	0	0.08	0.00002	-
10	3.16	2.30	40.6	0.00938	0.00408
20	6.32	4.59	82.9	0.0191	0.00415
30	9.48	6.89	126.6	0.0292	0.00423
40	12.6	9.19	171.7	0.0395	0.00430
50	15.8	11.5	218.4	0.0503	0.00438
60	19.0	13.8	266.5	0.0614	0.00445
70	22.1	16.1	316.2	0.0728	0.00453
80	25.3	18.4	367.3	0.0846	0.00460
90	28.5	20.7	419.9	0.0967	0.00468
100	31.6	23.0	474.1	0.1092	0.00475